Advanced Energy Materials

ADVANCED ENERGY MATERIALS
www.advenergymat.de

RESEARCH ARTICLE

Earth-Abundant Oxides Promoting High-Performance $Mg_3(Sb,Bi)_2$ Thermoelectrics via a Metathesis Strategy

Yi Wang[1,2] | Zhen Fan[1] | Kaiwei Guo[1,3] | Yunfan Li[1,3] | Dongheng Yang[1,4] | Fuhong Chen[1,5] | Xiaowei Wu[1,3] | Qi Zhao[1] | Joseph Woods[6] | Yuan Yao[1] | Yuan Yu[7] | Hangtian Zhu[1] | Lunhua He[1,8,9] | Duncan H Gregory[6] | Huaizhou Zhao[1]

[1]Beijing National Laboratory for Condensed Matter Physics, Institute of Physics, Chinese Academy of Sciences, Beijing, China | [2]College of Materials Science and Opto-Electronic Technology, University of Chinese Academy of Sciences, Beijing, China | [3]School of Physical Science, University of Chinese Academy of Sciences, Beijing, China | [4]Hebei Key Lab of Optic-Electronic Information and Materials, Key Laboratory of High-Precision Computation and Application of Quantum Field Theory of Hebei Province, College of Physics Science and Technology, Hebei University, Baoding, China | [5]School of Physics, Beijing Institute of Technology, Beijing, China | [6]WestCHEM, School of Chemistry, Joseph Black Building, University of Glasgow, Glasgow, UK | [7]Institute of Physics (IA), RWTH Aachen University, Aachen, Germany | [8]Spallation Neutron Source Science Center, Dongguan, China | [9]Songshan Lake Materials Laboratory, Dongguan, China

Correspondence: Zhen Fan (fanzhen@iphy.ac.cn) | Huaizhou Zhao (hzhao@iphy.ac.cn)

Received: 20 April 2026 | **Revised:** 24 August 2026 | **Accepted:** 1 September 2026

Keywords: chemical engineering | energy conversion efficiency | materials science | metathesis | thermoelectric effect | thermoelectric materials

ABSTRACT

The bright promise of $Mg_3(Sb,Bi)_2$ as a next-generation near-room-temperature thermoelectric material is challenged both by the need for reliable and economical synthesis and by performance degradation from detrimental Mg-vacancy defects at grain boundaries and within grains. Here, we reveal that Earth-abundant oxides (Fe_2O_3, ZrO_2 and TiO_2) can unlock superior thermoelectric performance in $Mg_3(Sb,Bi)_2$ via a simple metathesis strategy. Incorporation of the oxides (at only 1–3 mol%) in Mg-excess $Mg_3(Sb,Bi)_2$ powders during spark-plasma sintering initiates "Mg-oxide" reduction reactions; the subsequent "transition metal-$Mg_3(Sb,Bi)_2$" reactions release a source of additional Mg, whose global diffusion refills cationic vacancies in the bulk matrix, enabling markedly enhanced power factors and figures of merit. Our fabricated 8-pair $Mg_3Sb_{0.75}Bi_{1.25}$/MgAgSb device attained remarkable conversion efficiency and output power density of 11.7% and 1.0 W cm^{-2} at a temperature gradient (ΔT) of 315 K. Notably, a $Mg_3Sb_{0.5}Bi_{1.5}/Bi_{0.5}Sb_{1.5}Te_3$ module demonstrated maximum cooling ΔTs competitive with state-of-the-art Bi_2Te_3 coolers at 200–373 K. The proposed metathesis strategy not only offers an eco-friendly and cost-effective route to defect engineering, promoting applications of $Mg_3(Sb,Bi)_2$ TEs, but also provides key insights into the structure-property relationships and thermoelectric performance optimization of other Mg-based TEs and Zintl phases.

1 | Introduction

Thermoelectrics (TEs) enable a solid-state route for the direct conversion between heat and electricity [1–4]. The performance of TE materials is fundamentally determined by the dimensionless figure of merit (zT), $zT = S^2\sigma T/(\kappa_e + \kappa_L)$, where S, σ, T, κ_e, κ_L are the Seebeck coefficient, electrical conductivity, absolute temperature, and electronic and lattice-thermal conductivities, respectively [5]. Maximized electrical transport properties (e.g., the power factor, PF, $PF = S^2\sigma$) and minimized thermal

Yi Wang and Zhen Fan contributed equally to this work.

conductivities are thus essential toward high zTs. However, the above physical parameters are inherently intercoupled [3–5], making it challenging to optimize the zT of TEs. Bi_2Te_3-based materials, with remarkable near room-temperature (RT) performance, have remained the only commercialized TE material family to date, demonstrating unparalleled TE cooling and power-generation capabilities in near-RT applications over decades [6–8]. However, drawbacks including the high raw-material cost, sub-optimal mechanical properties, and limited zT values over a narrow temperature range have been viewed as significant constraints on their large-scale deployment [9–13]. Notably, n-type $Mg_3(Bi,Sb)_2$ has emerged as a promising next-generation TE candidate since the first report in 2016, featuring typical traits of high zTs (over a wider temperature range than Bi_2Te_3), mechanical robustness, low cost, and environmental friendliness [4, 12, 14–17]. Pioneering laboratory $Mg_3(Bi,Sb)_2$-based modules have progressively achieved excellent maximum cooling temperature differences rivaling those of Bi_2Te_3 (typically with the hot-side temperature of 300–400 K) as well as exceptionally high energy-conversion efficiencies of approximately 9–12% over a temperature gradient of ca. 300 K, demonstrating promising prospects in the near RT range [18–21].

One distinct obstacle that hinders the advancement of high-performance $Mg_3(Sb,Bi)_2$ has been identified as the existence and distribution of energetically favorable Mg vacancies in the matrix, which stem from the ease of Mg loss during material synthesis and subsequent sintering and fabrication processes [15]. Thermodynamic calculations and experimental studies reveal that these *Zintl* phases are not linear phases with a single stoichiometry; the Mg vacancies act as intrinsic acceptor defects (or electron "killers") and, particularly, serve as detrimental scattering centers for electrons [22]. Typically, excessive Mg and aliovalent doping at anion/cation sites are both required during synthesis to achieve n-type conduction [16, 23–30]. Nevertheless, studies suggest Mg vacancies still persist in the final sintered bulk materials, both inside crystal grains and at grain boundaries (GBs), resulting in inferior electrical transport properties (e.g., σ and PF) [31, 32].

Many contemporary investigations have been devoted to mitigating detrimental Mg-poor GBs. Despite strategies for minimizing GB density through the growth of coarse grains or single crystals, additive-based GB engineering has significantly enhanced charge-carrier transport and improved low-temperature zTs in polycrystalline $Mg_3(Sb,Bi)_2$ [19, 33–39]. These approaches include Mg_2Cu-aided sintering for GB composition and grain-size modulation [36], formation of GB complexions by Nb addition [37], nano- and the application of the transition-metal wetting/gating theory [38, 39]. Typically in this last approach, transition metals (e.g., Nb and Ta) and/or conductive TiO_{2-n} were often introduced during mechanochemical synthesis, and the formed "transition metal-$Mg_3(Sb,Bi)_2$" metal-semiconductor interfaces were proposed to reduce GB potential barriers for charge carriers, significantly promoting the decoupling of electrical and thermal transport [38, 39]. Nevertheless, a recent work indicated that the TE properties of the sintered $Mg_3(Sb,Bi)_2$ are highly sensitive to both the elemental composition of the additives and the route of their incorporation (e.g., at the synthesis or the sintering steps) [40]. Alternatively, prior long-term Mg vapor annealing treatment, e.g., at 600°C for 65 h, has been experimentally established as a Mg-vacancy remediation approach for sintered pellets and/or p-type single crystals of $Mg_3(Sb,Bi)_2$, enabling acoustic-phonon-dominated carrier transport in less-defective $Mg_3(Sb,Bi)_2$ *Zintls* without secondary-phase additives [34, 41]. However, more practical and efficient regulation mechanisms of Mg vacancies within the matrix grains remain poorly understood, although both recent research on magnesium-ion batteries and our own calculations have unraveled some of the aspects of Mg^{2+} diffusion kinetics within $P\bar{3}m1$ structured $Mg_3(Sb,Bi)_2$ lattices [21, 42]. Leveraging the three-dimensional Mg-ion diffusion in $Mg_3(Sb,Bi)_2$ characterized by low energy barriers, we previously demonstrated a "local-reaction global-diffusion" strategy [21]. Selected transition metals (*TM*s) triggered local reactions with the anionic components in $Mg_3(Sb,Bi)_2$ and generated excess Mg in situ, which effectively refilled matrix Mg vacancies through subsequent global diffusion within the $Mg_3(Sb,Bi)_2$ lattices, significantly promoting the electrical transport properties for the entire material system [21, 43].

The reliable and economic fabrication of high-performance bulk materials is one of the central requirements for the large-scale application of $Mg_3(Sb,Bi)_2$-based TEs. However, the methods aforementioned often necessitate complex intermetallics, expensive transition metals, and/or stringent processing conditions. Extending the interdisciplinary chemistry, physics, and materials understanding of $Mg_3(Sb,Bi)_2$ into a broader chemical space will therefore further facilitate its practical application potential. Herein, we demonstrate that Earth-abundant and cost-effective oxides (Fe_2O_3, ZrO_2, and TiO_2) can enable superior power-generation and cooling performance in n-type $Mg_3(Sb,Bi)_2$ via a simple metathesis chemistry approach (see the framework illustrated in Figure 1a by employing Fe_2O_3 as an example). By mixing the oxides with ball-milled Mg-excessive nominal "$Mg_{3.2}(Sb,Bi)_2$" powders, the in situ solid-state metathesis strategy proceeds progressively in three steps during subsequent spark plasma sintering (SPS) (Figure 1a): (i) the magnesothermal reduction reaction [44, 45], between excess Mg from the ball-milled powders and the *TM* oxides, reduces the oxides to the corresponding *TM*s; (ii) local reactions between the liberated *TM* species with the anionic component element(s) of the $Mg_3(Sb,Bi)_2$ matrix generate elemental Mg in situ; and (iii) the as-released elemental Mg effectively refills matrix Mg vacancies at the GBs and within grains via a rapid global diffusion process within minutes timescales. Accordingly, markedly enhanced carrier mobilities at 300 K (ca. 220 $cm^2\ V^{-1}s^{-1}$, which represents a value as high as comparable with single crystals), average PFs at 300–573 K (ca. 29 $\mu W\ cm^{-1}\ K^{-2}$, representing a 34 % increase over pristine $Mg_{3.2}Sb_{0.5}Bi_{1.497}Te_{0.003}$), and figures of merit were achieved for all oxide-incorporated $Mg_{3.2}Sb_{0.5}Bi_{1.497}Te_{0.003}$ (and $Mg_{3.2}Sb_{0.75}Bi_{1.247}Te_{0.003}$) (Figure 1a) [18, 19, 46, 47]. To verify the enhanced TE properties, an 8-pair $Mg_3Sb_{0.75}Bi_{1.25}$/MgAgSb device was fabricated, achieving high conversion efficiency and output power density of 11.7% and 1.0 $W\ cm^{-2}$, respectively, at a temperature gradient (ΔT) of 315 K, ranking among the highest values for full-Mg-based TE modules (Figure 1b) [20, 48–57]. In addition, a $Mg_3Sb_{0.5}Bi_{1.5}/Bi_2Te_3$ module demonstrated maximum cooling temperature differences—27.0, 46.8, 67.8, and 92.2 K at a hot-side temperature of 198, 250, 303, and 373 K, respectively—highly competitive to state-of-the-art Bi_2Te_3 coolers from sub-ambient to near-room temperatures at 200–373 K (Figure 1c) [18, 19, 55, 58–60]. The proposed metathesis strategy not only

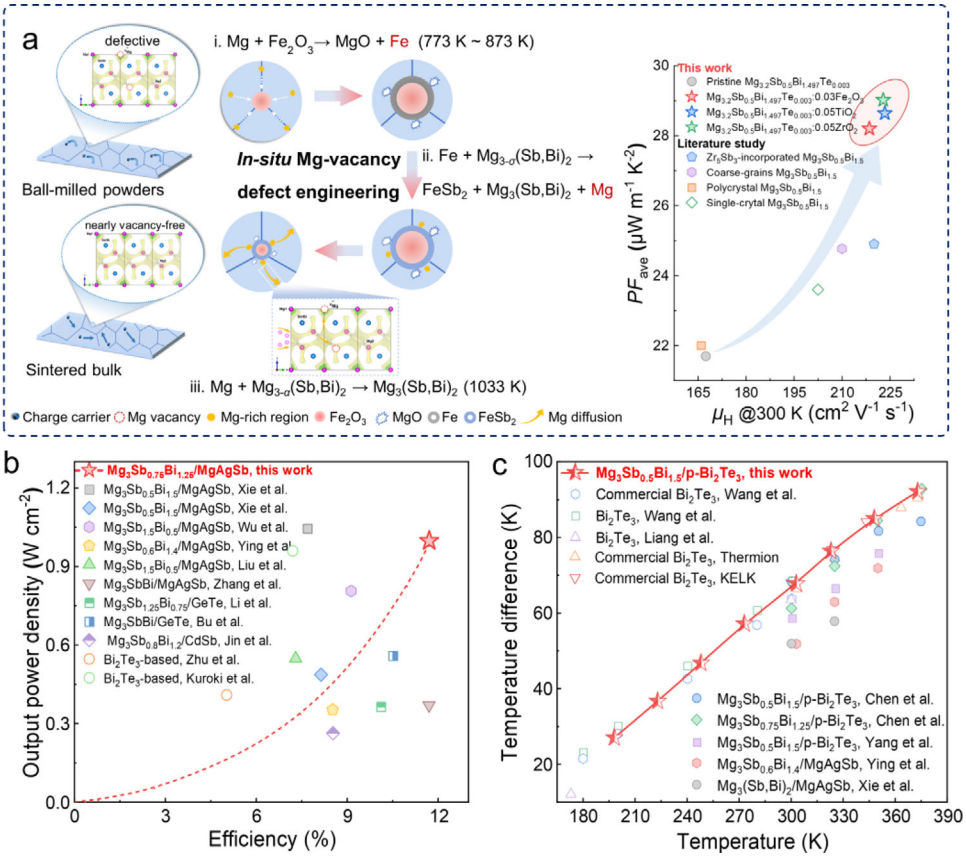

FIGURE 1 | Schematic strategy of the in situ Mg-vacancy defect engineering via the metathesis strategy and brief material transport properties and module performances of the vacancy-suppressed $Mg_3(Sb,Bi)_2$. (a) Schemtaic of the in situ solid-state metathesis chemistry and the corresponding enhancements in Hall mobility (at 300 K) and average *PF*s (at 300–573 K) for $Mg_{3.2}Sb_{0.5}Bi_{1.497}Te_{0.003}$ [18, 19, 46, 47]; (b) output power density versus efficiency plots of the $Mg_3Sb_{0.75}Bi_{1.25}$/MgAgSb module in comparison with recent literature studies [20, 48–57]; and (c) maximum cooling temperature differences of the $Mg_3Sb_{0.5}Bi_{1.5}/Bi_{0.5}Sb_{1.5}Te_3$ Peltier module compared to recent literature studies [18, 19, 55, 58–60]. The temperature gradients of literature modules in (b) were 300, 220, 300, 300, 315, 325, 265, 320, 320, 225, and 275 K, respectively (as captioned from top to bottom).

offers a facile and cost-effective route to regulating vacancy defects in $Mg_3(Sb,Bi)_2$, but also provides key insights into the structure-property relationships and thermoelectric performance optimization of other Mg-based TEs and *Zintl* phases.

2 | Results and Discussion

2.1 | Strategy Workflow Based on Lattice Mg^{2+} Diffusion and the Metathesis Concept

In this work, elemental precursors following the nominal "$Mg_{3.2}(Sb,Bi)_2$" stoichiometry were ball-milled, and trace amounts of Te (i.e., 0.15–0.25 at% at the Sb/Bi site) were adopted as the anionic dopant in all samples (full details available in the Experimental Section). Specific molar ratios of earth-abundant oxide powders (Fe_2O_3, TiO_2, and ZrO_2) were mixed with $Mg_{3.2}(Sb,Bi)_2$ powders after the ball-milling synthesis and sintered to promote the thermoelectric performance of the final $Mg_3(Sb,Bi)_2$ bulk samples. Although characterization results indicated the sub-stoichiometry of Mg for the sintered samples, the starting ratio (for example, $Mg_{3.2}Sb_{0.5}Bi_{1.497}Te_{0.003}$ and $Mg_{3.2}Sb_{0.5}Bi_{1.497}Te_{0.003}$:0.03$Fe_2O_3$) for all samples was used to keep the consistency and clarity for comparisons in materials characterization and transport properties. Our bond valence sum (BVS) and previous density functional theory (DFT) calculations suggested that three-dimensionally interconnected Mg^{2+} ionic diffusion channels with low energy barriers of ca. 0.2–0.6 eV exist in $Mg_3(Sb,Bi)_2$ *Zintls* (illustrated by the iso-surfaces of the Mg^{2+} potentials in Figure S1 for the $Mg_3Sb_{0.5}Bi_{1.5}$ composition) [21]. This lays the foundation for the refilling of surplus Mg into Mg-deficient $Mg_3(Sb,Bi)_2$ lattices (i.e., with intrinsic Mg vacancies) toward the thermodynamically more stable, less-defective $Mg_3(Sb,Bi)_2$, provided that additional Mg source(s) exist.

We first investigated the distribution and structure evolution of the excess Mg (which was introduced during ball-milling) in "$Mg_{3.2}(Sb,Bi)_2$" powders following the SPS process by varying the sintering temperature. *Ex situ* scanning electron microscopy (SEM) and elemental dispersive spectroscopy (EDS) results clearly identify the aggregation of elemental Mg metal particles of a few microns in size at low sintering temperatures of 673, 773, and 873 K, which are dispersed into the sintered bulk $Mg_{3.2}Sb_{0.5}Bi_{1.497}Te_{0.003}$ matrix (Figure S2a–c). By contrast, such Mg particles—segregated from the excess Mg starting material—were

not observed in the sample sintered at 1033 K (Figure S2d,e). SEM/EDS and Rietveld refinement results against experimental powder neutron diffraction (PND) data both indicate the Mg deficiency of the sintered sample, suggesting the existence of Mg vacancies in the bulk, which have been a typical defect acting as electron "killers" and abundant detrimental scattering sources of charge carriers (Figure S3) [21, 22]. The above results show that despite the excess Mg employed in the synthesis, the alloy experiences dynamic Mg loss during high-temperature sintering. There is evidently not sufficient Mg present to diffuse into the $Mg_{3-x}(Sb,Bi)_2$ lattice to repair the Mg vacancies in the $P\bar{3}m1$ structure of $Mg_3(Sb,Bi)_2$. These results agree with our recent work and literature studies (even with higher nominal Mg contents than $Mg_{3.2}(Sb,Bi)_2$), demonstrating the poor efficiency of merely adding excess Mg precursor during sample preparation [21, 22, 55].

Magnesothermal reduction is a well-established solid-state approach characterized by high reduction potential (−2.36 V vs. the standard hydrogen electrode), ease of handling, and low reaction temperatures (of ca. 500°C or lower) [44, 61]. The chemistry has been extensively employed in metallurgy, battery materials synthesis, and nanocomposite fabrication, etc. [45]. In light of our recent research on supplying additional Mg to defective $Mg_3(Sb,Bi)_2$ lattices during SPS by a selected group of *TM*s via the "local-reaction global diffusion" concept, we devise a solid-state "metathesis" concept herein (Figure 1a), that converts the excess Mg in $Mg_{3.2}(Sb,Bi)_2$ powders into *TM*s from their earth-abundant oxides (Fe_2O_3, TiO_2 and ZrO_2) at relatively low sintering temperatures. The formed corresponding *TM*s then induce local reaction and global diffusion processes at higher sintering temperatures, effectively mitigating the Mg-vacancy problem within minutes.

Control experiments were performed to validate the "Mg-oxide" magnesothermal reactions. Pellets constructed from consecutive layers of "Mg powder/Fe_2O_3 powder/Mg powder" were sintered under vacuum for 5 min at 673, 773, and 873 K, respectively (Figure S4). The *ex situ* SEM and EM characterization confirmed the onset of the magnesothermal reduction at a temperature no higher than 773 K, as indicated by the enrichment area of elemental Fe (as labeled in Figure S6). Notably, both dispersed elemental Fe particles and a layer of MgO were identified in Figure S7 (corresponding to the sintering temperature of 873 K). Subsequent thermogravimetric-differential thermal analyses (TG-DTA) of the $Mg_{3.2}Sb_{0.5}Bi_{1.497}Te_{0.003}$:0.03$TiO_2$ and $Mg_{3.2}Sb_{0.5}Bi_{1.497}Te_{0.003}$:0.03$ZrO_2$ powder mixtures started to exhibit exothermic behavior at ca. 723–823 K (Figure S9), affirming the exothermic magnesothermal reaction between the incorporated oxides and excess elemental Mg in the ball-milled $Mg_{3.2}(Sb,Bi)_2$ powders and agreeing with the SEM/EDS results in Figures S8 and S12. The obvious exothermic characteristics above 873 K are in line with the fact that the Mg-deficient $Mg_3(Sb,Bi)_2$-elemental Mg system tends to shift to a thermodynamically stable, less-defective $Mg_3(Sb,Bi)_2$ single phase [21]. Overall, the design of the in situ solid-state metathesis experiment was formulated as a step-wise process, proceeding as indicated below (see also Figure 1a):

$$TMO_z + z\,Mg \rightarrow z\,MgO + TM \quad (1)$$

$$x\,TM + Mg_{3-\sigma}(Sb_{\beta 1}Bi_{\beta 2})_2 \rightarrow [1-\sigma/3-y/2]\,Mg_3(Sb_{\gamma 1}Bi_{\gamma 2})_2 + TM_xSb_y + 3y/2\,Mg \quad (2)$$

$$\alpha\,Mg + Mg_{3-\alpha}(Sb,Bi)_2 \rightarrow Mg_3(Sb,Bi)_2 \quad (3)$$

It should be noted that, as Equation 2 generates TM_xSb_y products, the "*TM*-defective $Mg_{3-\sigma}(Sb,Bi)_2$" reaction leads to minor changes in the Sb/Bi ratio of the $Mg_3(Sb,Bi)_2$ main phase residing at the guest-host interfaces, where the anionic composition changes can be expressed as below:

$$[1-\sigma/3-y/2]\times 2\gamma_1 + y = 2\beta_1 \quad (4)$$

$$[1-\sigma/3-y/2]\times 2\gamma_2 = 2\beta_2 \quad (5)$$

Quantitatively determining the chemical composition of this local $Mg_3(Sb,Bi)_2$ phase remains challenging due to the challenges in temporally and spatially resolved in situ characterization techniques to date [62, 63]. Nonetheless, considering the very low incorporation content of oxides (of merely 1–3 mol%) and the nanometer-scale reaction depth, such local reactions do not affect the overall Sb/Bi ratio of the host $Mg_3(Sb,Bi)_2$ matrix, as suggested by the subsequent characterization results.

2.2 | Microstructure and Characterization

Scanning transmission electron microscopy (STEM) characterization was first performed to probe the "$Mg_{3.2}(Sb,Bi)_2$-*TM* oxide" interfacial chemistry and the microstructure & compositional evolution in the vicinity of such interfaces. For the $Mg_{3.2}Sb_{0.5}Bi_{1.497}Te_{0.003}$ sample incorporated with 3% Fe_2O_3 (molar ratio, noted as $Mg_{3.2}Sb_{0.5}Bi_{1.497}Te_{0.003}$:0.03$Fe_2O_3$), the low-resolution STEM and elemental mapping images in Figure 2a (and Figures S10 and S11) confirm the dispersion of Fe-containing guest particles (of ca. 500 nm in diameter) within the $Mg_{3.2}Sb_{0.5}Bi_{1.497}Te_{0.003}$ matrix (both within main-phase grain interiors and at grain boundaries), along with the formation of MgO nanoparticles, which confirms that the "Mg-Fe_2O_3" magnesothermal reaction has proceeded as anticipated (Equation 1). Meantime, the enrichment of Sb at the Fe regions (Figure 2a) supports the proposed "Fe-$Mg_{3-\sigma}(Sb,Bi)_2$" reaction step, which forms Fe-Sb intermetallics (Equation 2) and releases additional Mg for the subsequent refilling of Mg within defective $Mg_{3-\alpha}Sb_{0.5}Bi_{1.497}Te_{0.003}$ lattices (Equation 3). Figure 2b further illustrates that guest Fe_2O_3 particles formed clear interfaces with the host $Mg_{3.2}Sb_{0.5}Bi_{1.497}Te_{0.003}$ matrix. The high-resolution TEM images and corresponding Fast-Fourier-Transform (FFT) patterns (e.g., Figure 2c) demonstrate that $FeSb_2$ existed on one side of the guest-host interface (indicated by the FFT spots). The diffraction spots were indexed to the [0 1 $\bar{1}$], [$\bar{1}$ 0 1], and [1 $\bar{2}$ 1] lattice planes of $FeSb_2$, and the interplanar spacing of 2.81 Å matched the d-spacing of [0 1 $\bar{1}$] lattice fringes (Figure 2c1) [64]. The formation of $FeSb_2$ was in excellent agreement with our previous thermodynamic calculations and supportive of our designed local-reaction global-diffusion strategy toward Mg vacancy repairing as elaborated above [21]. At the matrix side of

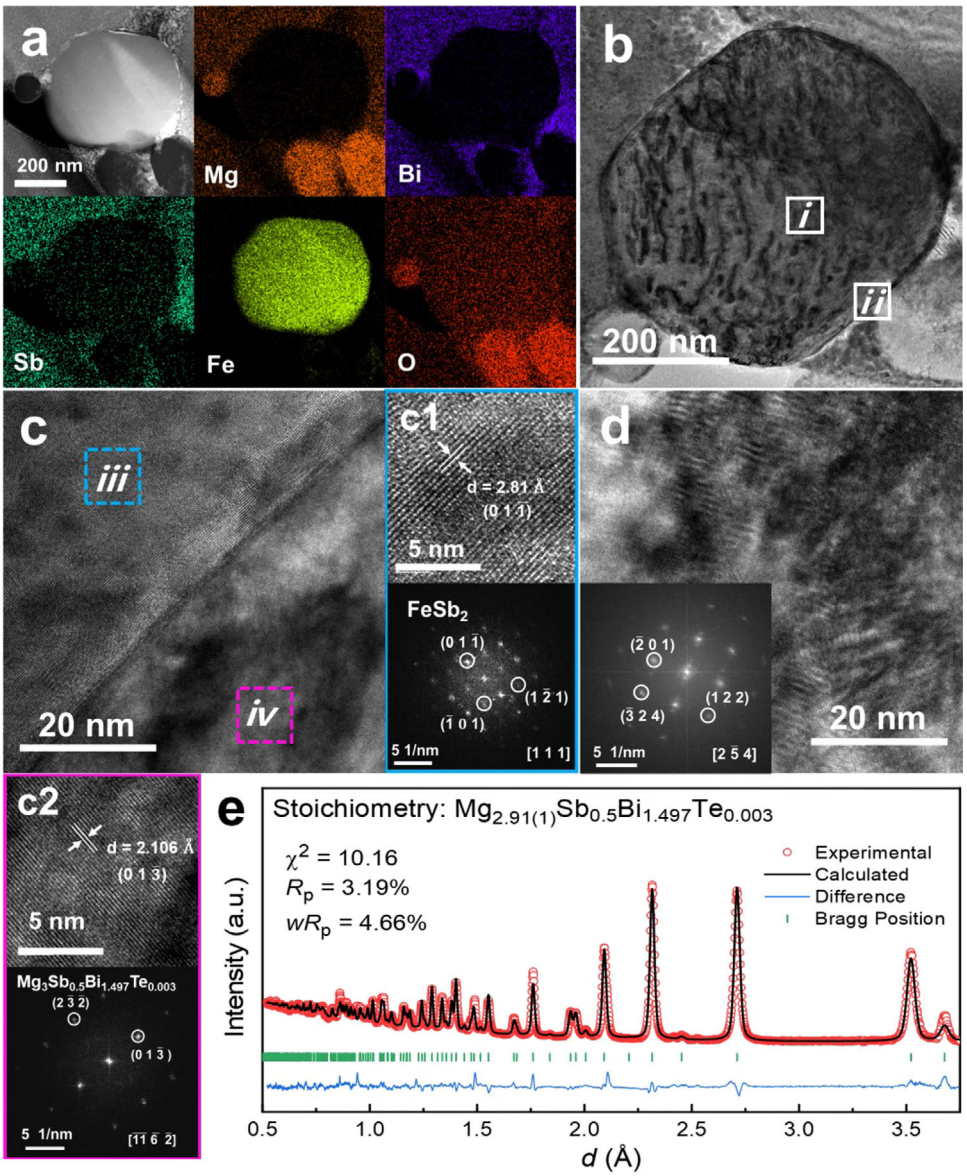

FIGURE 2 | Materials characterization of the $Mg_{3.2}Sb_{0.5}Bi_{1.497}Te_{0.003}$:0.03$Fe_2O_3$ sample post the SPS process at 1033 K. (a) Back-scattered SEM image and the corresponding EDS element maps; (b) mid-resolution STEM image of the "matrix and guest" region; (c) high-resolution STEM image of "region *ii*" in (b), with the high-resolution images and fast Fourier transform (FFT) diffractograms in the inset (*c1*) and (*c2*) corresponding to "region *iii*" and "region *iv*", respectively, in (c); (d) high-resolution STEM image of "region *i*" in (b); (e) profile plots of Rietveld refinement against the PND dataset of the $Mg_{3.2}Sb_{0.5}Bi_{1.497}Te_{0.003}$:0.03$Fe_2O_3$ sample.

the interface (Figure 2c2), a single-crystalline $Mg_3(Sb,Bi)_2$ phase was observed. The high-resolution TEM image and the inset FFT results in Figure 2d indicate that the host-guest metathesis chemistry mainly proceeded at the interfaces, as the crystal structure of Fe_2O_3 was resolved in the inner region of the guest Fe_2O_3 particle.

The above results agree well with our recent work, i.e., if additional Mg were provided, global diffusion would enable refilling Mg vacancies via long-range cationic diffusion both at grain boundaries and within inner grains [21]. Indeed, the Rietveld refinement against PND patterns reveals site-occupancy factors (SOFs) of 0.960(9) and 0.958(8) for Mg1 and Mg2 sites, respectively, with a stoichiometry of $Mg_{2.88(1)}Sb_{0.5}Bi_{1.497}Te_{0.003}$ for pristine $Mg_{3.2}Sb_{0.5}Bi_{1.497}Te_{0.003}$ (Figure S3c, Tables S1 and S2). In contrast, $Mg_{3.2}Sb_{0.5}Bi_{1.497}Te_{0.003}$:0.03$Fe_2O_3$ exhibited SOF(Mg1) and SOF(Mg2) of 0.981(11) and 0.965(9), respectively (Figure 2e; Tables S3 and S4), corresponding to a stoichiometry of $Mg_{2.91(1)}Sb_{0.5}Bi_{1.497}Te_{0.003}$. The PND results reinforce that the lattice Mg vacancies were effectively reduced at the atomic scale, affirming the metathesis chemistry and global diffusion in $Mg_3(Sb,Bi)_2$. Further STEM/EDS evidence proves that the metathesis chemistry and structural/compositional evolutions can be extended equally to the $Mg_{3.2}Sb_{0.5}Bi_{1.497}Te_{0.003}$:0.03$ZrO_2$ sample (Figure S12). Notably, the $Mg_{3.2}Sb_{0.5}Bi_{1.497}Te_{0.003}$:0.03$ZrO_2$ sample exhibited a core-shell structure at the host-guest interface (Figure S12), with the guest particles residing within main-phase grain interiors and with an insulating MgO shell encapsulating the inner Zr-Sb intermetallic core. This microstructural feature contrasts with that of the $Mg_{3.2}Sb_{0.5}Bi_{1.497}Te_{0.003}$:0.03$Fe_2O_3$

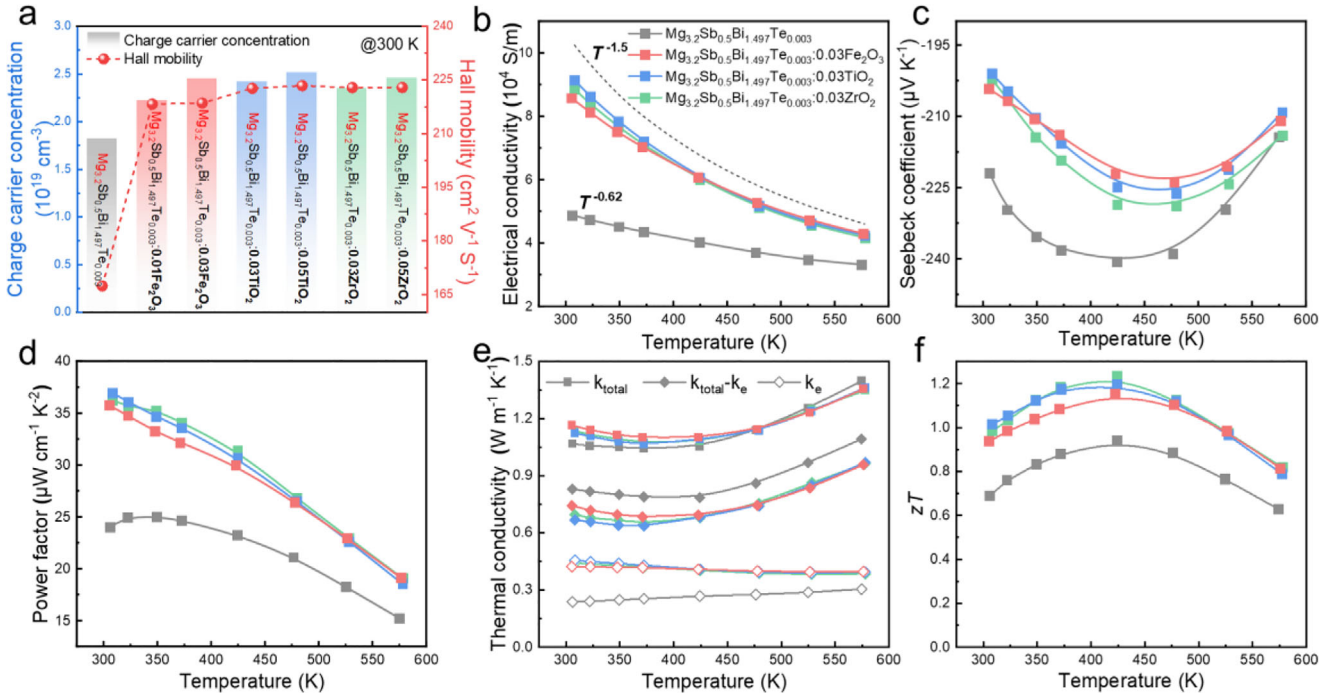

FIGURE 3 | Thermoelectric properties of vacancy-suppressed $Mg_{3.2}Sb_{0.5}Bi_{1.497}Te_{0.003}$ samples. Fe_2O_3-, TiO_2-, ZrO_2-incorporated and pristine Mg-Sb-Bi-Te samples are indicated by red, blue, green, and grey data markers, respectively. (a) Effects of Fe_2O_3, TiO_2 and ZrO_2 content on charge-carrier concentration and Hall mobility of $Mg_{3.2}Sb_{0.5}Bi_{1.497}Te_{0.003}$ samples; (b–f) electrical conductivity, Seebeck coefficient, power factor, thermal conductivities, and zT of the Fe_2O_3, TiO_2, and ZrO_2-incorporated $Mg_{3.2}Sb_{0.5}Bi_{1.497}Te_{0.003}$ samples versus temperature compared to pristine $Mg_{3.2}Sb_{0.5}Bi_{1.497}Te_{0.003}$, respectively.

sample. Given the electrically insulating nature of MgO, these microstructure characteristics in Figure 2 and Figures S10–S12, combined with the identical electrical conductivities and Seebeck coefficients below for both samples, confirm that the enhanced electrical properties stem from the reduced Mg vacancies in the bulk matrix, rather than the reduction of GB potential barriers by metal-semiconductor interfaces that were previously suggested [38, 39].

2.3 | Thermoelectric Properties and Transport Mechanisms

As might be anticipated from the Mg vacancy-filling design strategy, the transport properties of the modified samples varied significantly from pristine $Mg_{3.2}Sb_{0.5}Bi_{1.497}Te_{0.003}$. Figure 3a shows an obvious increase (of ca. 25%) in the charge-carrier concentration (n_H) for each of the Fe_2O_3-, TiO_2-, and ZrO_2-incorporated samples when compared to pristine $Mg_{3.2}Sb_{0.5}Bi_{1.497}Te_{0.003}$. This is consistent with the increase in Mg content as confirmed by the characterization evidence (Figure 2e; Figure S3c), affirming a reduction in bulk Mg vacancies. Indeed, this is in line with theoretical studies that relate charge-carrier concentration and/or carrier type to Mg vacancy concentration [22]. More specifically, the Hall mobility results in Figure 3a show that charge-carrier mobilities (μ_H) of ca. 220 cm^2 V^{-1} S^{-1} were achieved in the Fe_2O_3-, TiO_2-, and ZrO_2-incorporated samples as opposed to 167.4 cm^2 V^{-1} S^{-1} for pristine $Mg_{3.2}Sb_{0.5}Bi_{1.497}Te_{0.003}$. The carrier mobility in the modified samples therefore surpasses that in most polycrystalline and single-crystalline $Mg_3Sb_{0.5}Bi_{1.5}$ samples [18, 19, 46, 47]. Accordingly, the electrical conductivity (σ) reached ~9× 10^4 S m^{-1} at 303 K for all the oxide-incorporated samples, a twofold increase compared to that of 4.5× 10^4 S m^{-1} for pristine $Mg_{3.2}Sb_{0.5}Bi_{1.497}Te_{0.003}$. As opposed to the $T^{-0.62}$ trend in the σ evolution of pristine $Mg_{3.2}Sb_{0.5}Bi_{1.497}Te_{0.003}$ at 300–573 K, all oxide-incorporated samples exhibited an approximately $T^{-1.5}$ temperature dependence in σ. The quintessential acoustic phonon-dominated charge-carrier transport behavior confirms that the detrimental scattering from Mg vacancy defects has been effectively suppressed [19, 31, 34]. Considering the microstructures shown in Figure 2 and Figure S10–S12, the markedly enhanced charge carrier mobility and electrical conductivity suggest that a minor content of incorporated secondary phases, even electrically insulating MgO nanoparticles, has negligible impact on the electrical transport of the main $Mg_3(Sb,Bi)_2$ matrix. Given the increased carrier concentration, Figure 3c shows slightly reduced absolute Seebeck coefficient values at 300 K and the shift of bipolar conductivity toward higher temperatures for all the oxide-incorporated samples. The Pisarenko plot in Figure S13 indicates the same density-of-states effective mass (m_{dos}*) value (1.15 m_e) for both pristine and the oxide-incorporated $Mg_{3.2}Sb_{0.5}Bi_{1.497}Te_{0.003}$ samples. This suggests that our strategy only promotes μ_H (by suppressing Mg vacancies) and imposes no obvious effects on the intrinsic electronic band structure of $Mg_3(Sb,Bi)_2$. Consequently, the *PF*s of all the oxide-incoporated samples were almost identical (~36 μW cm^{-1} K^{-2} at 303 K) and were comparable to the values for Ti-incorporated samples that previously reported [21]. This corresponds to a 56% increase in the *PF* compared to pristine $Mg_{3.2}Sb_{0.5}Bi_{1.497}Te_{0.003}$ (Figure 3d). All the oxide-incorporated samples exhibited near-identical temperature-dependent power factors from 300 to

573 K. The corresponding average *PF* (PF_{ave}) values approached ~27 μW cm^{-1} K^{-2}, which is approximately 35% higher than that of pristine $Mg_{3.2}Sb_{0.5}Bi_{1.497}Te_{0.003}$ and ranks amongst the highest reported values for $Mg_3(Sb,Bi)_2$ materials (Figure 3d; Figures S14c, S15c, and S16c).

Based on the single-parabolic band modeling, the Lorenz number was derived from the experimental Seebeck coefficient (full details available in Supporting Information) [18, 19], and the electrical thermal conductivity (κ_e) was calculated according to the Wiedemann–Franz law [5]. The κ_e increased markedly with increasing σ for all the oxide-incorporated $Mg_{3.2}Sb_{0.5}Bi_{1.497}Te_{0.003}$ samples (Figure 3e). However, the measured total thermal conductivity only demonstrated a slight increase at 300–470 K for each of the oxide-incorporated samples compared to pristine $Mg_{3.2}Sb_{0.5}Bi_{1.497}Te_{0.003}$. Figure 3e illustrates that the clear reduction in the lattice thermal conductivity for the oxide-incorporated $Mg_{3.2}Sb_{0.5}Bi_{1.497}Te_{0.003}$ samples is responsible for this effect. The phenomena are in line with our previous study on *TM-incorporated* $Mg_3(Sb,Bi)_2$ samples and likely reflect the lattice anharmonicity of $Mg_3(Sb,Bi)_2$, consistent with other $Mg_3(Sb,Bi)_2$ materials modulated through defect engineering (e.g., via Mg-vapor annealing and GB-engineering with Nb) [19, 33–39]. The overall impacts of the introduced secondary phases (e.g., MgO and $FeSb_2$ byproducts from the in situ reaction) on charge carrier and phonon transport are different, although these localized nanoparticles at interfaces can act as impurity scattering centers [4, 8, 12]. The secondary phases with physical properties distinct from $Mg_3(Sb,Bi)_2$ may introduce acoustic mismatch and local strain fields within the host matrix, forming phonon-scattering centers [24, 29, 38, 39, 47]. Indeed, the enrichment of nanoscale secondary phases and the resulting high density of nanoscale interfaces have been reported to preferentially scatter low- and mid-frequency phonons [39, 65]. Meanwhile, the observed simultaneous boost in electrical conductivity and Hall mobility indicates the negligible effects of such dispersed nanoscale impurity phases on electrical transport, provided that the principally detrimental scattering caused by Mg vacancies has been effectively mitigated. Given the significantly enhanced electrical transport and the effectively suppressed lattice thermal conductivity, all the oxide-incorporated samples demonstrated superior zT values at 300–573 K compared to pristine $Mg_{3.2}Sb_{0.5}Bi_{1.497}Te_{0.003}$ (Figure 3f); notably, average zT (zT_{ave}) values from 300 to 573 K above unity were achieved (1.03 and 1.06 for Fe_2O_3 and TiO_2/ZrO_2 incorporated samples, respectively, Figures S14e, S15e, and S16e), which are ~25% higher than that of pristine $Mg_{3.2}Sb_{0.5}Bi_{1.497}Te_{0.003}$.

The metathesis strategy equally contributed to improved TE properties at temperatures below 300 K, as confirmed by transport properties of the $Mg_{3.2}Sb_{0.5}Bi_{1.497}Te_{0.003}$:0.03$Fe_2O_3$ sample from 140 to 300 K (Figure S17). Moreover, further experiments suggested the general applicability of our metathesis concept for $Mg_3(Sb,Bi)_2$ *Zintls* with different Sb/Bi ratios. Figure S18a shows the enhancement of σ in Fe_2O_3-incorporated $Mg_{3.2}Sb_{0.75}Bi_{1.25}$ samples from 303 to 573 K, leading to an elevated *PF* compared to pristine $Mg_3Sb_{0.75}Bi_{1.25}$ (Figure S18c). The addition of Fe_2O_3 also contributed to the decrease in κ_L (Figure S18d), resulting in the $Mg_{3.2}Sb_{0.75}Bi_{1.247}Te_{0.003}$:0.03$Fe_2O_3$ sample with a zT of 0.93 at 300 K, comparable to commercial n-type Bi_2Te_3. The $Mg_{3.2}Sb_{0.75}Bi_{1.245}Te_{0.005}$:0.03 Fe_2O_3 sample (with a higher carrier concentration) showed a peak zT of 1.46 at 473 K and an zT_{ave} of 1.31 over 300–573 K, demonstrating promising potential for near RT low-grade heat recovery applications (Figure S18e).

2.4 | Device-Level Performances of Power-Generation and Peltier Cooling Modules

Benefitting from the elevated zT_{ave} and PF_{ave} (300–573 K) of the $Mg_{3.2}Sb_{0.75}Bi_{1.245}Te_{0.005}$:0.03$Fe_2O_3$ sample, an 8-pair power-generation device was fabricated to validate the TE properties and its application potential (coupled with p-type MgAgSb, cross-section area of 1×1 cm^2, noted as the $Mg_3Sb_{0.75}Bi_{1.25}$/MgAgSb power-generation module, full details available in Supporting Information). The evolution in current-dependent electrical output voltage & power, heat flow, and TE conversion efficiency at different temperature gradients is shown in Figure 4a, Figure S19, and Figure 4b, respectively. The linear output voltage-current plots in Figure 4a serve to exemplify the function and response of our power-generation module. The maximum TE conversion efficiency reached 11.7% at ΔT = 315 K (in line with finite-element simulation results, Figure 4c) with a maximum output power density of 1.0 W cm^{-2}. This represents one of the highest-performing power-generation modules over this temperature range compared to previously reported efficiencies typically of ca. 7–11% and power densities generally no higher than ca. 0.7 W cm^{-2} (Figures 4c and 1b) [20, 48–57, 66]. Both the device internal resistance and the open-circuit voltage (at ΔT = 305 K) remained essentially unchanged after > 900 h of storage under an Ar atmosphere and periodic measurement under vacuum (Figure 4d). These characteristics highlight the robust stability of the high-efficiency, high-power-density device and its prospective use for low-grade heat recovery.

To demonstrate the potential of our oxide-incorporated $Mg_3(Sb,Bi)_2$ samples in solid-state cooling applications near RT and at sub-ambient temperatures, a 7-pair Peltier cooling device, based on $Mg_{3.2}Sb_{0.5}Bi_{1.497}Te_{0.003}$:0.03$Fe_2O_3$ and commercial p-type $Bi_{0.5}Sb_{1.5}Te_3$, was fabricated (cross-section area of 1×1 cm^2, noted as the $Mg_3Sb_{0.5}Bi_{1.5}/Bi_{0.5}Sb_{1.5}Te_3$ Peltier module, full details available in Supporting Information). The current-dependent cooling temperature difference curves at different hot-side temperatures (T_h) are shown in Figure 4e. In a T_h range of 300–373 K, which is normally reported for Peltier cooling devices, our device demonstrated maximum cooling temperature differences (ΔT_{max}) of 67.8, 76.4, 85.0, and 92.2 K at T_h of 303, 323, 348, and 373 K, respectively (Figure 4e). The ΔT_{max} values ranked among the highest values for $Mg_3(Sb,Bi)_2$-based coolers as reported in the literature (e.g., 52–61 K at T_h of around 300 K) and were comparable to state-of-the-art Bi_2Te_3 commercial coolers (e.g., ~90 K at T_h = 373 K) (Figure 1c) [18, 19, 55, 58]. Notably, we also demonstrate the cooling capabilities of $Mg_3(Sb,Bi)_2$-based materials at sub-ambient temperatures of 200–273 K. The attainable cooling ΔT_{max} reached 27.0, 36.6, 46.8, and 57.2 K at T_h of 198, 223, 248, and 273 K, respectively (Figures 4e and 1c). These results provide further confirmation of the excellent cryogenic cooling capability of our oxide-incorporated $Mg_3(Sb,Bi)_2$ materials and how a device-level performance boost can be unlocked via the metathesis strategy such that operation rivals that of conventional Bi_2Te_3 thermoelectric modules (Figure 1c) [59, 60]. Moreover, the device's internal

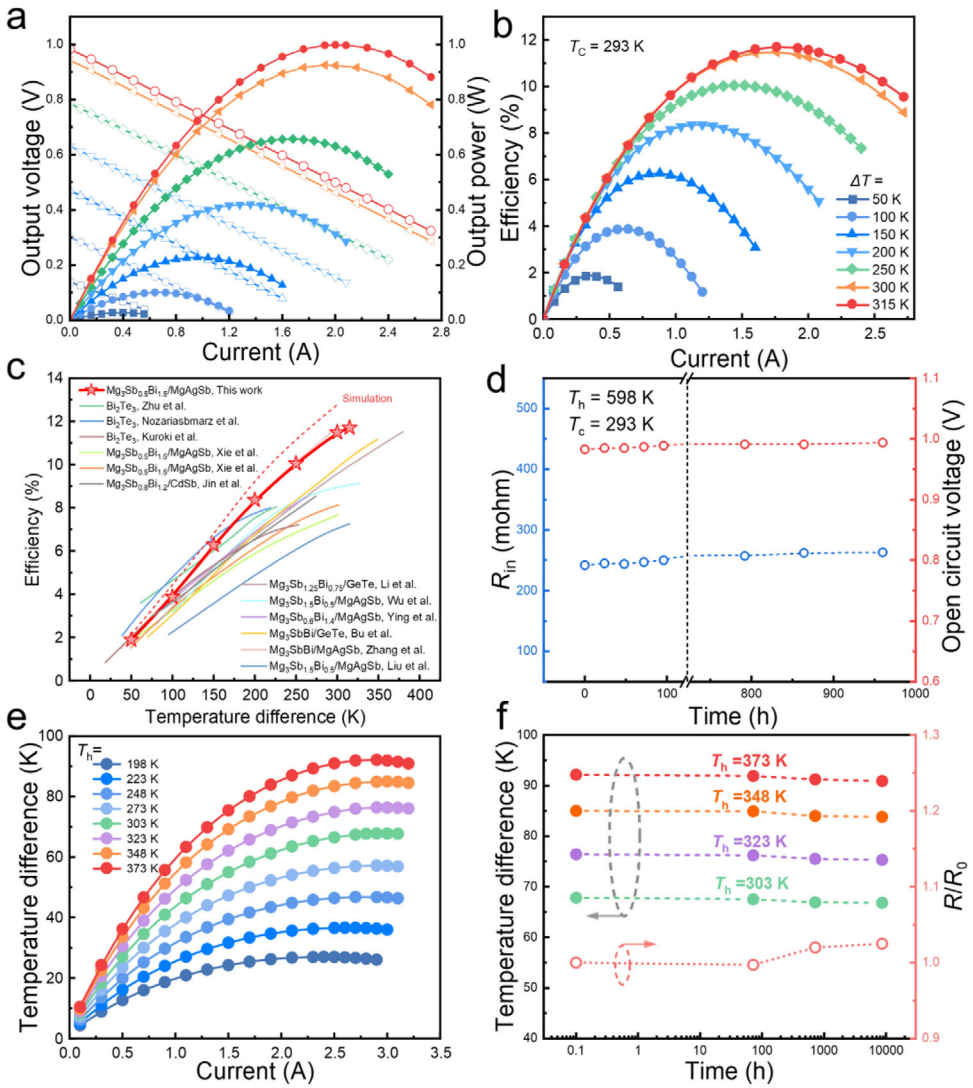

FIGURE 4 | Performance and durability of power-generation and thermoelectric cooling devices. (a,b) Evolution of output voltage, output power, and conversion efficiency versus current at different temperature gradients for a $Mg_3Sb_{0.75}Bi_{1.25}$/MgAgSb power-generation module; (c) thermoelectric conversion efficiencies at different temperature gradients for a $Mg_3Sb_{0.75}Bi_{1.25}$/MgAgSb power-generation module in comparison with recent literature studies [20, 48–57, 66]. (d) evolution of internal resistance and open-circuit voltage (T_h = 598 K, T_c = 293 K) over ~1,000 h; (e) cooling temperature differences of a $Mg_3Sb_{0.5}Bi_{1.5}/Bi_{0.5}Sb_{1.5}Te_3$ Peltier module versus current for a series of hot-side temperatures; (f) stability tests of cooling temperature difference and internal resistance for a $Mg_3Sb_{0.5}Bi_{1.5}/Bi_{0.5}Sb_{1.5}Te_3$ module.

resistance did not increase appreciably, and the ΔT_{max} remained stable after the module was stored under an Ar atmosphere for over 10,000 h (Figure 4f). Overall, the above results highlight the capability of $Mg_3(Sb,Bi)_2$ systems as stable high-performance TEs in solid-state cooling over a wide temperature range from 200 to 373 K.

3 | Conclusions

In conclusion, significant improvements in the performance of $Mg_3(Sb,Bi)_2$ thermoelectrics were enabled by introducing Earth-abundant oxides (Fe_2O_3, TiO_2 and ZrO_2, of only 1–3 mol%) via a metathesis strategy, through which the detrimental Mg vacancies as commonplace in pristine $Mg_3(Sb,Bi)_2$ were effectively modulated. Such defect mitigation led to markedly enhanced charge-carrier mobilities, a twofold increase in room-temperature electrical conductivity, drastically boosted electrical power factors, and much-improved figures-of-merit; all instigated by the adoption of an acoustic phonon-dominated charge-carrier transport mechanism. Accordingly, an 8-pair power-generation device constructed from the materials achieved a high conversion efficiency and an output power density of 11.7% and 1.0 W cm^{-2}, respectively, under a temperature gradient of 315 K, ranking among the highest values for full-Mg-based TE modules. The in situ Mg vacancy engineering process also had striking effects on the low-temperature thermoelectric properties. A fabricated Peltier module demonstrated maximum cooling ΔT values that were highly competitive with state-of-the-art Bi_2Te_3 coolers from sub-ambient to near-room temperatures at 200–373 K. The proposed metathesis strategy offers an eco-friendly and cost-effective approach to defect engineering, facilitating the large-scale application of $Mg_3(Sb,Bi)_2$ thermoelectrics. Furthermore, it provides key insights into the structure-property relationships

and thermoelectric performance optimization of other Mg-based TEs and *Zintl* phases.

4 | Experimental

High-purity Mg turnings (99.8%, Alfa Aesar), Bi chunks (99.99%, Alfa Aesar), Sb shots (99.99%, Alfa Aesar), and Te powders (325 mesh, 99.5%, Adamas) were weighed according to the compositions of $Mg_{3.2}Sb_xBi_{2-x-y}Te_y$ (in molar ratios of the starting materials) in an Ar-gas-filled glovebox. The elemental precursors with a total mass of 10 g were loaded into a stainless-steel ball-milling jar in the glovebox (with the oxygen and water level below 0.1 ppm). High-energy ball milling was conducted for 10 h for each synthesis using a SPEX 8000D mill. For $Mg_{3.2}Sb_xBi_{2-x-y}Te_y$ without the incorporation of transition metal oxides, the ball-milled powders were transferred into a graphite die (inner diameter of 12.7 mm) inside the glovebox and sintered at 1033 K for 5 min under vacuum. For $Mg_{3.2}Sb_xBi_{2-x-y}Te_y$ samples incorporating transition metal oxides, Fe_2O_3, ZrO_2, and TiO_2 powders were weighed and mixed with ball-milled $Mg_{3.2}Sb_xBi_{2-x-y}Te_y$ powders using a pair of mortar and pestle in molar ratios of $Mg_{3.2}Sb_xBi_{2-x-y}Te_y$: *z TMO* and sintered under the same conditions as the *TM* oxides-free samples. Detailed characterization, property measurement, calculation method, and module fabrication and test information are provided in Supplementary Materials.

Resource Availability

Further information and requests for resources and materials should be directed to and will be fulfilled by the lead contact, **Huaizhou Zhao** (hzhao@iphy.ac.cn).

Author Contributions

Z.F., Y.W., and H.Z.Z. conceived the metathesis strategy. D.H.G. validated the metathesis strategy. Y.W. and Z.F. prepared the $Mg_3(Sb,Bi)_2$-based materials and performed experimental characterization and measurements. Y.W. and Z.F. performed the BVS calculations and performed transport modelling. Y.W, X.W.W, and F.H.C. conducted low-temperature thermoelectric property measurements. Y.F.L., Y.W., and Z.F. conducted the finite-element simulation of the power-generation module. K.W.G. and D.H.Y. provided p-type MgAgSb TE legs. Y.W., Z.F., and K.W. Guo constructed modules; Q.Z. provided experimental support. Y.Y. and Y.W. conducted TEM characterization and analysis. J.W. and D.H.G. performed the TG-DTA measurement. D.H.G contributed to data analysis and discussion. H.T.Z. and Y.Y. provided experimental support and valuable discussion. Y.W., Z.F., and L.H.H. performed PND experiments and Rietveld refinement. Y.W. and Z.F. analyzed all data. Y.W. and Z.F. drafted the original paper; Z.F., H.Z.Z., and D.H.G. conducted review and revisions. Z.F., H.T.Z., and H.Z.Z. provided funding acquisition. All authors contributed helpful discussions to this work.

Acknowledgements

The authors acknowledge the funding support of the Beijing Science and Technology Research Plan (Grant No. Z231100006623002). Z.F. and H.Z.Z. thank the Chinese Academy of Sciences (CAS) for the grant under the CAS Specific Research Associate Funding program for Z.F. D.H.G. acknowledges the University of Glasgow for a PhD studentship for J.W. The authors thank the China Spallation Neutron Source for the granted beam time on the General Purpose Powder Diffractometer (https:/cstr.cn/31113.02.CSNS.GPPD) and the beamline scientist Dr. Huaile Lu for the assistance. This work is supported by the Research Platform of Material Genome and the Synergic Extreme Condition User Facility in Huairou, Beijing, China.

Conflicts of Interest

The authors declare no conflicts of interest.

Data Availability Statement

The data that support the findings of this study are available from the corresponding author upon reasonable request.

References

1. D. M. Rowe, *CRC Handbook of Thermoelectrics*, 1st ed. (CRC Press, 1995), https://doi.org/10.1201/9781420049718.

2. F. DiSalvo, "Thermoelectric Cooling and Power Generation," *Science* 285 (1999): 703–706, https://doi.org/10.1126/science.285.5428.703.

3. G. J. Snyder and E. S. Toberer, "Complex Thermoelectric Materials," *Nature Materials* 7 (2008): 105–114, https://doi.org/10.1038/nmat2090.

4. Q. Lou, J. Gong, Z. Zang, et al., "Recent Advances and Challenges in Thermoelectrics Toward Near-Room-Temperature and High-Temperature Applications," *Chemical Society Reviews* 55 (2026): 2265–2324, https://doi.org/10.1039/d5cs01211b.

5. G. S. Nolas, J. Sharp, and J. Goldsmid, *Thermoelectrics: Basic Principles and New Materials Developments* (Springer, 2013), https://doi.org/10.1093/acprof:oso/9780195111668.001.0001.

6. I. T. Witting, T. C. Chasapis, F. Ricci, et al., "The Thermoelectric Properties of Bismuth Telluride," *Advanced Electronic Materials* 5 (2019): 1800904, https://doi.org/10.1002/aelm.201800904.

7. J. Pei, B. Cai, H. L. Zhuang, and J. F. Li, "Bi_2Te_3-Based Applied Thermoelectric Materials: Research Advances and New Challenges," *National Science Review* 7 (2020): 1856–1858, https://doi.org/10.1093/nsr/nwaa259.

8. X. L. Shi, J. Zou, and Z. G. Chen, "Advanced Thermoelectric Design: From Materials and Structures to Devices," *Chemical Reviews* 120 (2020): 7399–7515, https://doi.org/10.1021/acs.chemrev.0c00026.

9. L. D. Zhao, B. P. Zhang, J. F. Li, H. L. Zhang, and W. S. Liu, "Enhanced Thermoelectric and Mechanical Properties in Textured n-Type Bi_2Te_3 Prepared by Spark Plasma Sintering," *Solid State Sciences* 10 (2008): 651–658, https://doi.org/10.1016/j.solidstatesciences.2007.10.022.

10. T. S. Kim, I. S. Kim, T. K. Kim, S. J. Hong, and B. S. Chun, "Thermoelectric Properties of p-Type 25%Bi_2Te_3+75%Sb_2Te_3 Alloys Manufactured by Rapid Solidification and Hot Pressing," *Materials Science and Engineering: B* 90 (2002): 42–46, https://doi.org/10.1016/S0921-5107(01)00826-1.

11. W. He, D. Wang, H. Wu, et al., "High Thermoelectric Performance in Low-Cost $SnS_{0.91}Se_{0.09}$ Crystals-Cost $SnS_{0.91}Se_{0.09}$ Crystals," *Science* 365 (2019): 1418–1424, https://doi.org/10.1126/science.aax5123.

12. Y. Yan, W. Zhang, H. Kang, et al., "Advances and Challenges for $Mg_3(Sb,Bi)_2$-Based Thermoelectric Materials and Devices," *Journal of Materials Chemistry A* 14 (2026): 9065–9087, https://doi.org/10.1039/d5ta07320k.

13. M. A. Green, "Estimates of Te and in Prices From Direct Mining of Known Ores," *Progress in Photovoltaics: Research and Applications* 17 (2009): 347–359, https://doi.org/10.1002/pip.899.

14. J. Mao, H. Zhu, Z. Ding, et al., "High Thermoelectric Cooling Performance of n-Type Mg_3Bi_2-Based Materials," *Science* 365 (2019): 495–498, https://doi.org/10.1126/science.aax7792.

15. A. Li, C. Fu, X. Zhao, and T. Zhu, "High-Performance $Mg_3Sb_{2-x}Bi_x$ Thermoelectrics: Progress and Perspective," *Research* 2020 (2020): 1934848, https://doi.org/10.34133/2020/1934848.

16. H. Tamaki, H. K. Sato, and T. Kanno, "Isotropic Conduction Network and Defect Chemistry in $Mg_{3+\delta}Sb_2$-Based Layered Zintl Compounds With High Thermoelectric Performance," *Advanced Materials* 28 (2016): 10182–10187, https://doi.org/10.1002/adma.201603955.

17. J. Zhang, L. Song, S. H. Pedersen, H. Yin, L. T. Hung, and B. B. Iversen, "Discovery of High-Performance Low-Cost n-Type Mg_3Sb_2-Based Thermoelectric Materials With Multi-Valley Conduction Bands," *Nature Communications* 8 (2017): 13901, https://doi.org/10.1038/ncomms13901.

18. J. Yang, G. Li, H. Zhu, et al., "Next-Generation Thermoelectric Cooling Modules Based on High-Performance $Mg_3(Bi,Sb)_2$ Material," *Joule* 6 (2022): 193–204, https://doi.org/10.1016/j.joule.2021.11.008.

19. N. Chen, H. Zhu, G. Li, et al., "Improved Figure of Merit at Low Temperatures for Superior Thermoelectric Cooling in $Mg_3(Bi,Sb)_2$," *Nature Communications* 14 (2023): 4932, https://doi.org/10.1038/s41467-023-40648-5.

20. X. Zhang, H. Zhu, X. Dong, et al., "High-Performance $MgAgSb/Mg_3(Sb,Bi)_2$-Based Thermoelectrics With $\eta = 12\%$ at $T \leq 583K$," *Joule* 8 (2024): 3324–3335, https://doi.org/10.1016/j.joule.2024.08.013.

21. Z. Fan, Y. Wang, T. Lu, et al., "Local Reaction-Global Diffusion Unlocks High-Performance $Mg_3(Sb,Bi)_2$-Based Thermoelectrics," *Science Bulletin* 71 (2025): 1043–1054, https://doi.org/10.1016/j.scib.2025.11.037.

22. S. Ohno, K. Imasato, S. Anand, et al., "Phase Boundary Mapping to Obtain n-Type Mg_3Sb_2-Based Thermoelectrics," *Joule* 2 (2018): 141–154, https://doi.org/10.1016/j.joule.2017.11.005.

23. K. Liu, C. Chen, X. Li, et al., "Tuning the Carrier Scattering Mechanism by Rare-Earth Element Doping for High Average zT in Mg_3Sb_2-Based Compounds," *ACS Applied Materials & Interfaces* 14 (2022): 7022–7029, https://doi.org/10.1021/acsami.1c23395.

24. L. Wang, N. Sato, Y. Peng, et al., "Realizing High Thermoelectric Performance in N-Type $Mg_3(Sb,Bi)_2$-Based Materials via Synergetic Mo Addition and Sb–Bi Ratio Refining," *Advanced Energy Materials* 13 (2023): 2301667, https://doi.org/10.1002/aenm.202301667.

25. J. Mao, J. Shuai, S. Song, et al., "Manipulation of Ionized Impurity Scattering for Achieving High Thermoelectric Performance in n-Type Mg_3Sb_2-Based Materials," *Proceedings of the National Academy of Sciences* 114 (2017): 10548–10553, https://doi.org/10.1073/pnas.1711725114.

26. Z. Han, Z. Gui, Y. B. Zhu, et al., "The Electronic Transport Channel Protection and Tuning in Real Space to Boost the Thermoelectric Performance of $Mg_{3+\delta}Sb_{2-y}Bi_y$ Near Room Temperature," *Research* 2020 (2020): 1672051, https://doi.org/10.34133/2020/1672051.

27. X. Shi, T. Zhao, X. Zhang, et al., "Extraordinary n-Type Mg_3SbBi Thermoelectrics Enabled by Yttrium Doping," *Advanced Materials* 31 (2019): 1903387, https://doi.org/10.1002/adma.201903387.

28. J. Zhang, L. Song, A. Mamakhel, M. R. V. Jørgensen, and B. B. Iversen, "High-Performance Low-Cost n-Type Se-Doped Mg_3Sb_2-Based *Zintl* Compounds for Thermoelectric Application," *Chemistry of Materials* 29 (2017): 5371–5383, https://doi.org/10.1021/acs.chemmater.7b01746.

29. J.-S. Liang, X.-L. Shi, Y. Peng, et al., "Synergistic Effect of Band and Nanostructure Engineering on the Boosted Thermoelectric Performance of n-Type $Mg_{3+\delta}(Sb,Bi)_2$ *Zintls*," *Advanced Energy Materials* 12 (2022): 2201086, https://doi.org/10.1002/aenm.202201086.

30. F. Zhang, C. Chen, H. Yao, et al., "High-Performance N-Type Mg_3Sb_2 Towards Thermoelectric Application Near Room Temperature," *Advanced Functional Materials* 30 (2020): 1906143, https://doi.org/10.1002/adfm.201906143.

31. J. J. Kuo, Y. Yu, S. D. Kang, O. Cojocaru-Mirédin, M. Wuttig, and G. J. Snyder, "Mg Deficiency in Grain Boundaries of n-Type Mg_3Sb_2 Identified by Atom Probe Tomography," *Advanced Materials Interfaces* 6 (2019): 1900429, https://doi.org/10.1002/admi.201900429.

32. J. J. Kuo, S. D. Kang, K. Imasato, et al., "Grain Boundary Dominated Charge Transport in Mg_3Sb_2-Based Compounds," *Energy & Environmental Science* 11 (2018): 429–434, https://doi.org/10.1039/c7ee03326e.

33. T. Kanno, H. Tamaki, H. K. Sato, et al., "Enhancement of Average Thermoelectric Figure of Merit by Increasing the Grain-Size of $Mg_{3.2}Sb_{1.5}Bi_{0.49}Te_{0.01}$," *Applied Physics Letters* 112 (2018): 033903, https://doi.org/10.1063/1.5016488.

34. M. Wood, J. J. Kuo, K. Imasato, and G. J. Snyder, "Improvement of Low-Temperature zT in a Mg_3Sb_2–Mg_3Bi_2 Solid Solution via Mg-Vapor Annealing," *Advanced Materials* 31 (2019): 1902337, https://doi.org/10.1002/adma.201902337.

35. Q.-Q. Wang, K.-F. Liu, Y.-Y. Su, et al., "High Thermoelectric Performance and Anisotropy Studies of N-Type Mg_3Bi_2-Based Single Crystal," *Acta Materialia* 255 (2023): 119028, https://doi.org/10.1016/j.actamat.2023.119028.

36. J. Lei, K. Zhao, J. Liao, et al., "Approaching Crystal's Limit of Thermoelectrics by Nano-Sintering-Aid at Grain Boundaries," *Nature Communications* 15 (2024): 6588, https://doi.org/10.1038/s41467-024-50946-1.

37. T. Luo, J. J. Kuo, K. J. Griffith, et al., "Nb-Mediated Grain Growth and Grain-Boundary Engineering in Mg_3Sb_2-Based Thermoelectric Materials," *Advanced Functional Materials* 31 (2021): 2100258, https://doi.org/10.1002/adfm.202100258.

38. J.-W. Li, Z. Han, J. Yu, et al., "Wide-Temperature-Range Thermoelectric N-Type $Mg_3(Sb,Bi)_2$ With High Average and Peak zT Values," *Nature Communications* 14 (2023): 7428, https://doi.org/10.1038/s41467-023-43228-9.

39. J.-W. Li, H. Gao, Z. Han, et al., "In Situ Engineering of Grain Boundary Phase Toward Superior Thermoelectric Performance in $Mg_3(Sb,Bi)_2$," *Advanced Materials* 37 (2025): 2503665, https://doi.org/10.1002/adma.202503665.

40. L. F. Jiang, P. Xie, and S. Y. Tan, "From Doping to Composite Incorporation: Pathway-Dependent Carrier and Phonon Transport in Mg3 (Sb, Bi) 2," *Journal of Magnesium and Alloys* 21 (2026): 102131.

41. K. Imasato, C. G. Fu, Y. Pan, et al., "Metallic n-Type Mg_3Sb_2 Single Crystals Demonstrate the Absence of Ionized Impurity Scattering and Enhanced Thermoelectric Performance," *Advanced Materials* 32 (2020): 1908218, https://doi.org/10.1002/adma.201908218.

42. R. Mohtadi, O. Tutusaus, T. S. Arthur, Z. Zhao-Karger, and M. Fichtner, "The Metamorphosis of Rechargeable Magnesium Batteries," *Joule* 5 (2021): 581–617, https://doi.org/10.1016/j.joule.2020.12.021.

43. L. M. Zhang, L. Zhang, N. H. Li, Y. L. Yang, X. L. Shi, and Z. G. Chen, "Advances in Magnesium-Based Thermoelectrics: A Critical Review," *Advanced Materials* 0 (2026): 73493, https://doi.org/10.1002/adma.73493.

44. G. Zhu, W. Luo, L. Wang, W. Jiang, and J. Yang, "Silicon: Toward Eco-Friendly Reduction Techniques for Lithium-Ion Battery Applications," *Journal of Materials Chemistry A* 7 (2017): 24715–24737, https://doi.org/10.1039/c9ta08554h.

45. Y. Zhang, Z. Z. Fang, Y. Xia, et al., "Hydrogen Assisted Magnesiothermic Reduction of TiO_2," *Chemical Engineering Journal* 308 (2017): 299–310, https://doi.org/10.1016/j.cej.2016.09.066.

46. S. Zhou, Y. R. Yin, Y. Tian, et al., "Mg-Defect Compensation to Realize High Performance at Room Temperature in Mg_3Bi_2-Based Thermoelectric Single Crystals," *ACS Applied Materials & Interfaces* 16 (2024): 28886–28895, https://doi.org/10.1021/acsami.4c05443.

47. Q. Zhang, Z. Fan, X. Zhang, et al., "Enhancing $Mg_3(Bi,Sb)_2$ Thermoelectric Performance via $ZrSb_{1-x}$ Modified Grain-Boundary," *Materials Today Physics* 54 (2025): 101733, https://doi.org/10.1016/j.mtphys.2025.101733.

48. T. Kuroki, K. Kabeya, K. Makino, et al., "Thermoelectric Generation Using Waste Heat in Steel Works," *Journal of Electronic Materials* 43 (2014): 2405–2410, https://doi.org/10.1007/s11664-014-3094-5.

49. Z. Bu, X. Zhang, Y. Hu, et al., "A Record Thermoelectric Efficiency in Tellurium-Free Modules for Low-Grade Waste Heat Recovery," *Nature Communications* 13 (2022): 237, https://doi.org/10.1038/s41467-021-27916-y.

50. X. Li, C. Chen, L. Yin, et al., "Realizing an Excellent Conversion Efficiency of 14.5% in the Mg_3Sb_2/GeTe-Based Thermoelectric Module for Waste Heat Recovery," *Energy & Environmental Science* 16 (2023): 6147–6154, https://doi.org/10.1039/d3ee02587j.

51. X. Wu, Y. Lin, C. Liu, et al., "A High-Performance Eco-Friendly MgAgSb-Based Thermoelectric Power Generation Device Near Phase Transition Temperatures," *Energy & Environmental Science* 17 (2024): 2879–2887, https://doi.org/10.1039/d4ee00019f.

52. L. Xie, G. Peng, Y. Sun, et al., "Semiconductor–Semimetal Composite Engineering Enabling Record-High Thermoelectric Power Density for Low-Temperature Energy Harvesting," *Advanced Functional Materials* 34 (2024): 2401763, https://doi.org/10.1002/adfm.202401763.

53. B. Zhu, X. Liu, Q. Wang, et al., "Realizing Record High Performance in n-Type Bi_2Te_3-Based Thermoelectric Materials," *Energy & Environmental Science* 13 (2020): 2106–2114, https://doi.org/10.1039/d0ee01349h.

54. K. Jin, H. Nie, F. Gao, et al., "Thermo-Electro-Magnetic Interactions and ≈1 nm Fe Interfacial Layer Realize High Average ZT in Fe/$Mg_3(Sb,Bi)_2$ Below 300 °C," *Advanced Functional Materials* 35 (2024): 2418041, https://doi.org/10.1002/adfm.202418041.

55. P. Ying, L. Wilkens, H. Reith, et al., "A Robust Thermoelectric Module Based on MgAgSb/$Mg_3(Sb,Bi)_2$ With a Conversion Efficiency of 8.5% and a Maximum Cooling of 72 K," *Energy & Environmental Science* 15 (2022): 2557–2566, https://doi.org/10.1039/d2ee00883a.

56. Z. Liu, N. Sato, W. Gao, et al., "Demonstration of Ultrahigh Thermoelectric Efficiency of ∼7.3% in Mg_3Sb_2/MgAgSb Module for Low-Temperature Energy Harvesting," *Joule* 5 (2021): 1196–1208, https://doi.org/10.1016/j.joule.2021.03.017.

57. L. Xie, L. Yin, Y. Yu, et al., "Screening Strategy for Developing Thermoelectric Interface Materials," *Science* 382 (2023): 921–928, https://doi.org/10.1126/science.adg8392.

58. L. Xie, J. Yang, Z. Liu, et al., "Highly Efficient Thermoelectric Cooling Performance of Ultrafine-Grained and Nanoporous Materials," *Materials Today* 65 (2023): 5–13, https://doi.org/10.1016/j.mattod.2023.03.021.

59. K. Liang, H. Yang, P. Zhao, et al., "Characterizing the Thermoelectric Cooling Performance Across a Broad Temperature Range," *Review of Scientific Instruments* 94 (2023): 105112, https://doi.org/10.1063/5.0165551.

60. X. Wang, Z. Chen, S. Zhang, et al., "Enhanced Cryogenic Thermoelectric Cooling of $Bi_{0.5}Sb_{1.5}Te_3$ by Carrier Optimization," *InfoMat* 7 (2025): 12663, https://doi.org/10.1002/inf2.12663.

61. *Standard Potentials at 25°C* (Chemical 301, 2013) https://ch301.cm.utexas.edu/data/standard-potentials.php.

62. Z. Fan, W. R. Liu, L. Sun, et al., "Carbon-Free Conversion of SiO_2 to Si via Ultra-Rapid Alloy Formation: Toward the Sustainable Fabrication of Nanoporous Si for Lithium-Ion Batteries," *ACS Applied Materials & Interfaces* 15 (2023): 36076–36085, https://doi.org/10.1021/acsami.3c02197.

63. Z. Fan, M. D. Cappelluti, and D. H. Gregory, "Ultrafast, Energy-Efficient Synthesis of Intermetallics; Microwave-Induced Metal Plasma (MIMP) Synthesis of Mg2Sn," *ACS Sustainable Chemistry & Engineering* 7 (2019): 19686–19698, https://doi.org/10.1021/acssuschemeng.9b04811.

64. A. Kjekshus, P. G. Peterzens, T. Rakke, and A. F. Andersen, "Compounds With the Marcasite Type Crystal Structure. XIII. Structural and Magnetic Properties of Cr(t)Fe(1-t)As2, Cr(t)Fe(1-t)Sb2, Fe(1-t)Ni(t)As2 and Fe(1-t)Ni(t)Sb2," *Acta Chemica Scandinavica* 33 (1979): 469–480, https://doi.org/10.3891/acta.chem.scand.33a-0469.

65. G. Wu, A. R. Li, L. Q. Wang, X. Z. Wu, X. Y. Wang, and T. Mori, "Modulating Phonon Dynamics: Tailoring Lattice Vibrations to Enhance Thermoelectric Efficiency in $Mg_3(Sb, Bi)_2$ Alloy," *Nature Communications* 16 (2025): 10366, https://doi.org/10.1038/s41467-025-65325-7.

66. A. Nozariasbmarz, B. Poudel, W. J. Li, H. B. Kang, H. T. Zhu, and S. Priya, "Bismuth Telluride Thermoelectrics With 8% Module Efficiency for Waste Heat Recovery Application," *iScience* 23 (2020): 101340, https://doi.org/10.1016/j.isci.2020.101340.

Supporting Information

Additional supporting information can be found online in the Supporting Information section.

Supporting File: aenm71563-sup-0001-SuppMat.docx.